Journal of Geophysical Research: Space Physics

RESEARCH ARTICLE
10.1029/2018JA025400

Monte Carlo Simulations of the Interaction of Fast Proton and Hydrogen Atoms With the Martian Atmosphere and Comparison With In Situ Measurements

D. V. Bisikalo[1], V. I. Shematovich[1], J.-C. Gérard[2], and B. Hubert[2]

[1]Institute of Astronomy of the Russian Academy of Sciences, Moscow, Russia, [2]Laboratoire de Physique Atmosphérique et Planétaire, STAR Institute, Université de Liège, Liège, Belgium

Key Points:
- We present results from a kinetic Monte Carlo model of proton and hydrogen atom precipitation into the Martian atmosphere
- Comparison of simulations with SWIA MAVEN data makes it possible to infer the efficiency of charge exchange between solar wind and H corona
- Discrepancy with the measured spectra suggests that some of physical processes are not understood or that additional data should be analyzed

Correspondence to:
D. V. Bisikalo,
bisikalo@inasan.ru

Citation:
Bisikalo, D. V., Shematovich, V. I., Gérard, J.-C., & Hubert, B. (2018). Monte Carlo simulations of the interaction of fast proton and hydrogen atoms with the Martian atmosphere and comparison with in situ measurements. *Journal of Geophysical Research: Space Physics*, *123*, 5850–5861. https://doi.org/10.1029/2018JA025400

Received 26 FEB 2018
Accepted 11 JUN 2018
Accepted article online 19 JUN 2018
Published online 20 JUL 2018

Abstract We present model results of the interaction of proton and hydrogen atom precipitation with the Martian atmosphere. We use a kinetic Monte Carlo model developed earlier for the analysis of the Analyzer of Space Plasmas and Energetic Atoms (ASPERA-3) Mars Express data. With the availability of Mars Atmosphere and Volatile Evolution Mission in situ measurements, not only the flux of protons incident on the atmosphere but also their degradation along the orbit may now be described. The comparison of the simulations with data collected with the Solar Wind Ion Analyzer shows that the Monte Carlo model reproduces some of the measured features. The results of comparison between simulations and measurements of the proton fluxes at low altitudes make it possible to infer the efficiency of charge exchange between solar wind and the extended hydrogen corona if the value of the magnetic field is measured simultaneously. We also find that the induced magnetic field plays a very important role in the formation of the backscattered flux and strongly controls its magnitude. At the same time, discrepancies between the modeled and the measured energy spectra of the backscattered protons are pointed out. We suggest that some of the physical processes controlling the upward flux are not fully understood or that the data processing of the measured backscattered proton flux should be improved.

1. Introduction

The magnetosphere of Mars is unlike any other in our solar system, though it has aspects in common with many solar system objects. Mars has no strong global magnetic field, which allows the solar wind to interact directly with its exosphere and upper atmosphere. However, it has crustal magnetic fields strong enough to perturb the solar wind interaction. Mars' relatively weak gravity allows the formation of an extended exosphere, which leads to an upstream interaction in some ways reminiscent of a cometary environment. The end result is a complex and highly variable magnetosphere, with a mix of induced and intrinsic magnetic fields. Observations with the Spectroscopy for Investigation of Characteristics of the Atmosphere of Mars (SPICAM) instrument on Mars Express (MEX; Bertaux et al., 2005; Leblanc et al., 2006; Ritter et al., 2018) and the Imaging UltraViolet Spectrograph (IUVS) onboard the Mars Atmosphere and Volatile Evolution Mission (MAVEN) spacecraft (Deighan et al., 2016; Schneider et al., 2015, AGU Fall meeting 2016) have identified three types of aurorae on Mars, two of them (diffuse and proton aurorae) profoundly different from comparable types on Earth and other planets.

Two types of ultraviolet aurorae excited by energetic electrons were recently discovered on the Mars nightside. The first one (*discrete aurora*) was assigned to the structures of the residual magnetic field in the southern hemisphere (Bertaux et al., 2005; Leblanc et al., 2006). The main characteristics of the discrete aurorae were deduced from observations performed with the SPICAM instrument onboard MEX (Gérard et al., 2015). *The diffuse aurora* represents a second type of Martian auroral emission. It was observed on several occasions with the IUVS spectrograph in the wavelength range from 110 to 340 nm (Schneider et al., 2015). This aurora covers a large fraction of the planet in comparison with the very localized discrete aurora. Its brightness peaks near 65 km, which is significantly lower than the peak altitude (~140 km) for the discrete aurora (Soret et al., 2016). The occurrence of this diffuse aurora is directly related to enhanced solar activity in the far ultraviolet and the precipitation of high-energy (up to 200 keV) electrons into the Martian upper atmosphere. These aurorae are created by the precipitation of energetic electrons but, unlike the discrete aurora, they are thought to cover most of the planet for as long as the Sun sustains energetic outbursts, while

discrete aurorae are confined in space and time. This has significant implications for the energy budget of the middle atmosphere (Shematovich et al., 2017).

Finally, observations with the SPICAM instrument (Ritter et al., 2018) and the IUVS spectrograph (Deighan et al., 2016, Fall AGU meeting) have identified a third type, *proton aurora*, on Mars' dayside as an excess hydrogen Lyman-α emission confined to Mars' thermosphere. The intermittent additional brightness appears correlated with enhanced solar wind flux conditions. These observations dispel a common misconception that aurora only occurs near the lines of planetary magnetic fields. While this is true for the terrestrial aurora and the discrete aurora on Mars, it does not apply to the Martian diffuse and proton aurorae. In this sense, Mars serves as the best archetype for auroral processes on unmagnetized planets in our solar system and beyond. In contrast to previous auroral detections at Mars, the proton aurora is exclusively observed on the dayside and is characterized by enhanced hydrogen Lyman-α emission (121.6 nm) confined to the 120–150 km altitude range in limb viewing observations (Deighan et al., 2016, AGU Fall meeting 2016; Ritter et al., 2018). Peak emissions are up to 50% brighter than the optically thick dayglow background across the dayside and typically last a few hours or less. These events appear as strongly correlated with solar wind activity and the population of penetrating solar wind protons in the daytime thermosphere previously identified by the Solar Wind Ion Analyzer (SWIA) onboard MAVEN (Halekas et al., 2015).

The Martian exosphere (or "corona") is mainly populated by atomic and molecular hydrogen and extends up to many Martian radii (Chaufray et al., 2008). Therefore solar wind protons collide with neutral hydrogen in the extended corona and, following charge exchange and form a flux of fast hydrogen atoms with a velocity distribution similar to the original solar wind velocity spectrum. Its flux magnitude is of the order of 1–3% of the solar wind (Barabash et al., 1995; Galli et al., 2008; Holmström et al., 2002; Kallio et al., 1997; Wang et al., 2013, 2014). These energetic hydrogen atoms (H ENAs) enter the Mars thermosphere where they are repeatedly excited through elastic collisions, electron stripping, and charge exchange reactions, emitting Lyman-α photons when they are in neutral 2p excited state. Thus, unlike most auroral emissions, these photons originate from the precipitating particles themselves. While there is no exact terrestrial analog to the Martian phenomenon, it bears similarities to the cusp proton aurora, where the solar wind has localized access to the Earth's thermosphere (Frey et al., 2002; Gérard et al., 2001) and dayside equatorial precipitation of energetic neutrals produced in the ring current (Stephan et al., 2000). The solar wind protons are mostly deflected around the obstacle—the induced magnetosphere of Mars. At the same time the high-energy hydrogen atoms newly created in charge exchange collisions are not forced by electromagnetic fields and therefore can penetrate deep into the atmosphere where they collide with atmospheric gases. These processes result in angular spreading, energy deposition, and backscattering of a fraction of the precipitating flux of H ENAs (Kallio & Barabash, 2001; Shematovich et al., 2011). These hydrogen ENAs, together with H atoms produced in the solar wind and magnetosheath (Gunell et al., 2006) and the backscattered population (Futaana et al., 2006; Mura et al., 2008; Wang et al., 2013, 2014), were observed in the Martian system by the ASPERA-3 instrument onboard MEX. A fraction of the hydrogen atoms (both incoming and backscattered) interact with the atmosphere in charge-exchange reactions and become protons again. The altitude of the peak energy deposition is well below the MEX periapsis altitude of ~270 km; the MEX/ASPERA-3 observations of protons inside the Martian magnetosphere probably represent penetration of hot ions from the magnetosheath, because at MEX periapis, no protons were observed (Diéval et al., 2012, 2013). According to Halekas, Lillis, et al. (2015), the highest penetrating proton density with nearly the solar wind velocity was observed by MAVEN at periapsis (~160 km) in the dayside thermosphere, which is also the location of the highest CO_2 density along the orbit. This is consistent with charge exchange and electron stripping of incoming neutral particles in the Martian atmosphere (Kallio & Barabash, 2001; Shematovich et al., 2011).

In this study, we examine the interaction of proton and hydrogen atom precipitation into the Martian atmosphere. For this purpose, we use a kinetic Monte Carlo model including all major physical processes combined with in situ measurements by Halekas, Lillis, et al. (2015) of the downward proton fluxes from the magnetosheath at the upper boundary of the modeled atmosphere. We then compare the results of the calculations of the degradation of the incoming flux as a function of altitude with in situ data collected by the MAVEN/SWIA instrument (Halekas et al., 2015). This instrument was designed to measure ions with energies of 30 eV to 25 keV both in the upstream solar wind and within the Martian magnetosphere. Finally, we draw some conclusions about the importance of the backscattered component and the role of the induced magnetic field in the control of the magnitude of the backscattered component.

2. Brief Description of the Kinetic Monte Carlo Model

Precipitating high-energy hydrogen atoms and protons lose their kinetic energy in the following collisions:

$$H^+(H) + M \rightarrow \begin{cases} H^+_{f'}(H_{f'}) + M^* & (a) \\ H^+_{f'}(H_{f'}) + M^+ + e & (b) \\ H_{f'}\left(H^+_{f'}\right) + M^+(M) + (e). & (c) \end{cases}$$

with the neutral atmospheric gas. Here M denotes the major atmospheric constituents—CO_2, N_2, and O—included in the model. The different channels correspond to (a) the momentum and energy transfer in elastic and inelastic collisions, (b) ionization of target atmospheric molecules/atoms, and (c) charge transfer and electron capture collisions. Secondary fast $H_{f'}$ atoms and $H^+_{f'}$ protons carry enough kinetic energy to cycle through the collisional channels listed above. Such collisional cycling results in a growing set of translationally and internally excited atmospheric atoms and/or molecules M^*.

To study the precipitation of high-energy H/H^+ flux into the atmosphere, we solve the kinetic Boltzmann equations (Shematovich et al., 2011) for H^+ and H, including the collision term:

$$\mathbf{v}\frac{\partial}{\partial \mathbf{r}} f_{H/H+} + \left(\mathbf{g} + \frac{e}{m_{H+}}\mathbf{v}\times\mathbf{B}\right)\frac{\partial}{\partial \mathbf{v}} f_{H/H+} = Q_{H/H+}(\mathbf{v}) + \sum_{M=O,N_2,CO_2} J_{mt}\left(f_{H/H+}, f_M\right). \quad (1)$$

Equation (1) is written in the standard form for the velocity distribution functions $f_{H/H+}(\mathbf{r},\mathbf{v})$ for hydrogen atoms and protons and f_M $(\mathbf{r},\mathbf{v})$ for atmospheric gas (Gérard et al., 2000). The source term $Q_{H/H+}$ describes the production rate of secondary H/H^+ particles, and the elastic and inelastic collisional terms J_{mt} for H/H^+ describe the energy and momentum transfer to the ambient atmospheric gas (Shematovich et al., 1994) which is characterized by local Maxwellian velocity distribution functions. Our kinetic direct simulation Monte Carlo model (Bisikalo et al., 1995; Gérard et al., 2000; Shematovich et al., 1994, 2011) is used to solve kinetic equation (1). We used the 1-D approach for space and 3-D for velocities. The details of the model implementation and description of accuracy of the model (below 10%) can be found in Shematovich (2008). It should be pointed out that a key aspect of this model is the probabilistic treatment of the scattering angle distribution, which influences both the energy degradation rate and the angular redistribution of the precipitating protons (Bisikalo et al., 2017; Shematovich et al., 2017).

The region under study is limited by the lower boundary which is placed at 80 km, where H/H^+ particles are efficiently thermalized. The upper boundary is set at 500 km, where measurements of the precipitating protons were made by the SWIA instrument (Halekas, Lillis, et al., 2015). All detailed description of the model numerical aspects used in this study was given in recent papers (Bisikalo et al., 2017; Shematovich et al., 2017). The CO_2, CO, and O density profiles and temperature are taken from (Fox & Hac, 2009) for a low level of solar activity and are shown in Figure 1a. The temperature at 300 km is 139 K, and a change of atmospheric scale height is observed near 120 km where the temperature starts increasing with altitude.

In the Monte Carlo simulations presented hereafter, we assume that the horizontal induced magnetic field is constant in time and uniform in space. Field intensity values of $B = 0$, 15, 20, and 30 nT were used for the different runs, in agreement with the range of values measured at Mars by the Mars Global Surveyor (Brain et al., 2003), the MEX orbiters (Akalin et al., 2010), and MAVEN (Connerney et al., 2015).

3. Results of Monte Carlo Simulations

Mars Atmosphere and Volatile Evolution Mission's low altitude periapsis now provides an opportunity to measure the products of hydrogen ENAs penetrating deep in the Martian atmosphere. In this section, we model both the proton and hydrogen precipitation using in situ measurements of precipitating fluxes at the top of atmosphere as input parameters of the model. Further comparisons with measurements made at lower altitudes (near periapsis) allow us to draw some conclusions about the Martian atmosphere and the model validity.

3.1. Proton Precipitation

The first case we consider in the simulation corresponds to the proton energy spectrum measured in the magnetosheath and was taken from bottom right panel of Figure 1 in Halekas, Lillis, et al. (2015); see also

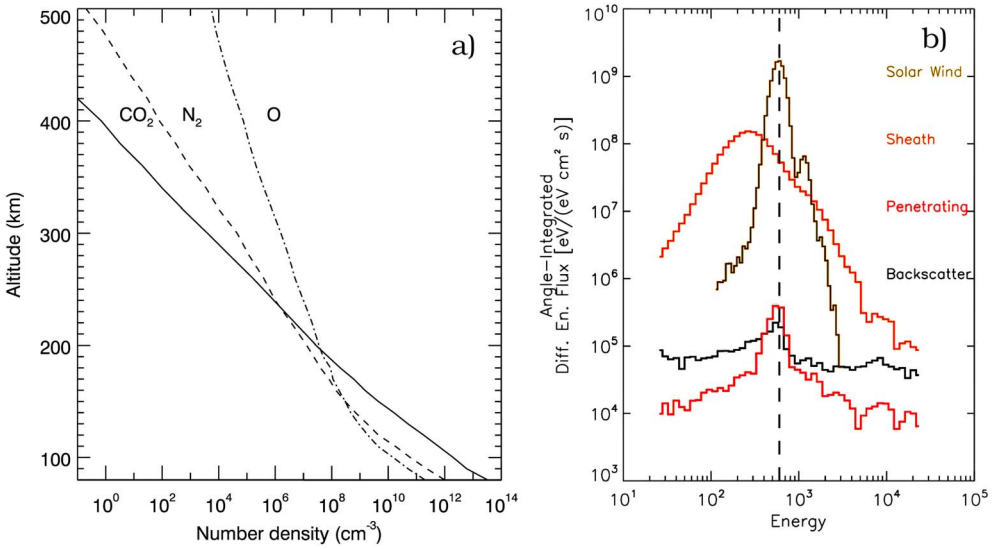

Figure 1. Model input data: (a) CO_2, CO, and O density profiles are taken from Fox and Hac (2009); (b) angle-integrated proton spectra from the solar wind (brown line) and angle-integrated proton spectra from the magnetosheath (orange line) were taken from the bottom right panel of Figure 1 in Halekas, Lillis, et al. (2015). The red and black lines correspond to penetrating and backscattered populations near periapsis at 160 km for 27 February 2015. The vertical dashed line corresponds to the peak of the undisturbed solar wind protons at 600 eV.

Figure 1b (orange line). These measurements were made on 27 February 2015 during an orbit near the terminator, in a region of very weak crustal magnetic fields. This case was chosen as a typical one where we can use both measured proton spectra of solar wind and magnetosheath.

The calculated differential upward H and H^+ number fluxes at 500 km for runs without and with induced horizontal magnetic field B = 0, 15, 20, and 30 nT are presented in Figure 2. The magnetosheath proton precipitation spectrum used as an input at the upper boundary in the simulations is shown by the orange line.

It is clearly seen that the presence of the induced magnetic field plays a very important role in the formation of the backscattered flux. The total upward energy fluxes of H and H^+ are respectively equal to 1.9% and 4.3% of the incident proton energy flux for the simulation without induced magnetic field. These fractions change to 0.4% and 19% for B = 15 nT, 0.2% and 22% for B = 20 nT, and 0.06% and 25% for B = 30 nT. This increase of the backscattered proton flux by a factor of 5 is caused by the shielding effect of the horizontal component of induced magnetic field (Shematovich et al., 2011). The gyroradii of the precipitating protons become smaller than the altitude range (~300 km) needed for protons to reach the collision-dominated region (below 200 km) of the Martian atmosphere.

To compare with the observations, we present the calculated upward and downward H^+ fluxes at 160 km in Figure 3 for cases without and for different values of the induced horizontal magnetic field. The input magnetosheath proton energy spectrum used in calculations is shown by the orange lines. The Monte Carlo calculations allow us to follow the flux degradation and for the first time to make a direct comparison with the flux measured near periapsis (see Figure 1b).

The simulations indicate that the absolute values of the penetrating fluxes are in a reasonable agreement with measurements at small magnetic fields, while it significantly decreases if the magnetic field increases. The peak energy for the case without magnetic field is at 200 eV, while it shifts to 1,000 eV in the case with B = 15 nT. The strong dependence of the peak position with the intensity of the induced magnetic field is a key result of these simulations, while it is not clearly seen in current observations. This is confirmed by the case for B = 30 nT where the peak moves to as much as 2,000 eV. The general shapes of the penetrating flux are different from the one measured by SWIA at periapsis (see Figure 1b). In the simulations we can see that the high energy wing is similar to the shape of the energy spectra of the penetrating flux from the magnetosheath. We note some depletion of the low energetic wing that is caused by collisional spreading of the penetrating flux and the formation of the backscattered flux.

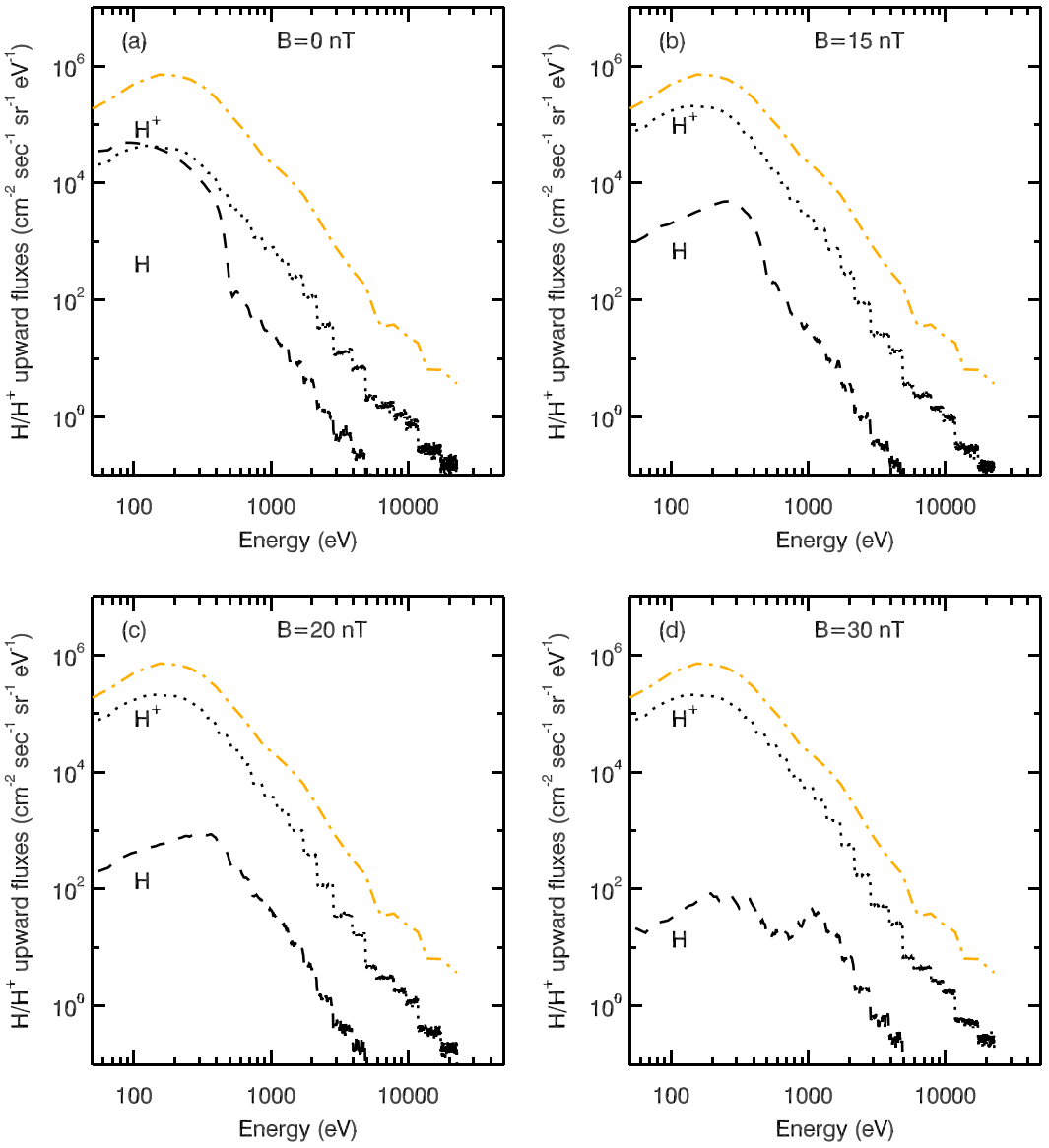

Figure 2. Upward H (dashed line) and H^+ (dotted line) fluxes at 500 km for the case of proton precipitation (a) without and with induced magnetic field (b) B = 15, (c) 20, and (d) 30 nT. The orange line shows the energy spectrum of the precipitating magnetosheath proton flux.

The peak value of the backscattered flux (black line) is in all cases a few times lower than the penetrating flux. The shape of the backscattered flux is radically different from the observed backscattered flux (see Figure 1b). The low energy wing is much larger than the high energy wing due to the process of collisional spreading of the penetrating protons.

3.2. Hydrogen Atom Precipitation

As mentioned earlier, precipitation of neutral hydrogen atoms is considered as a possible explanation for the characteristics of the energy distribution of the penetrating proton measured with SWIA such as the shape of the wings and the relative magnitude of the downward and upward fluxes. We examine this assumption by simulating fast hydrogen atom precipitation. In the simulation we use the proton flux from solar wind measured during the 27 February 2015 orbit (see Figure 1b), also shown by the green lines in Figures 4 and 5. According to the estimates by Kallio et al. (1997), in the model, the spectrum of the precipitating hydrogen atoms was taken equal to 1% of the angle-integrated ion spectrum from the solar wind.

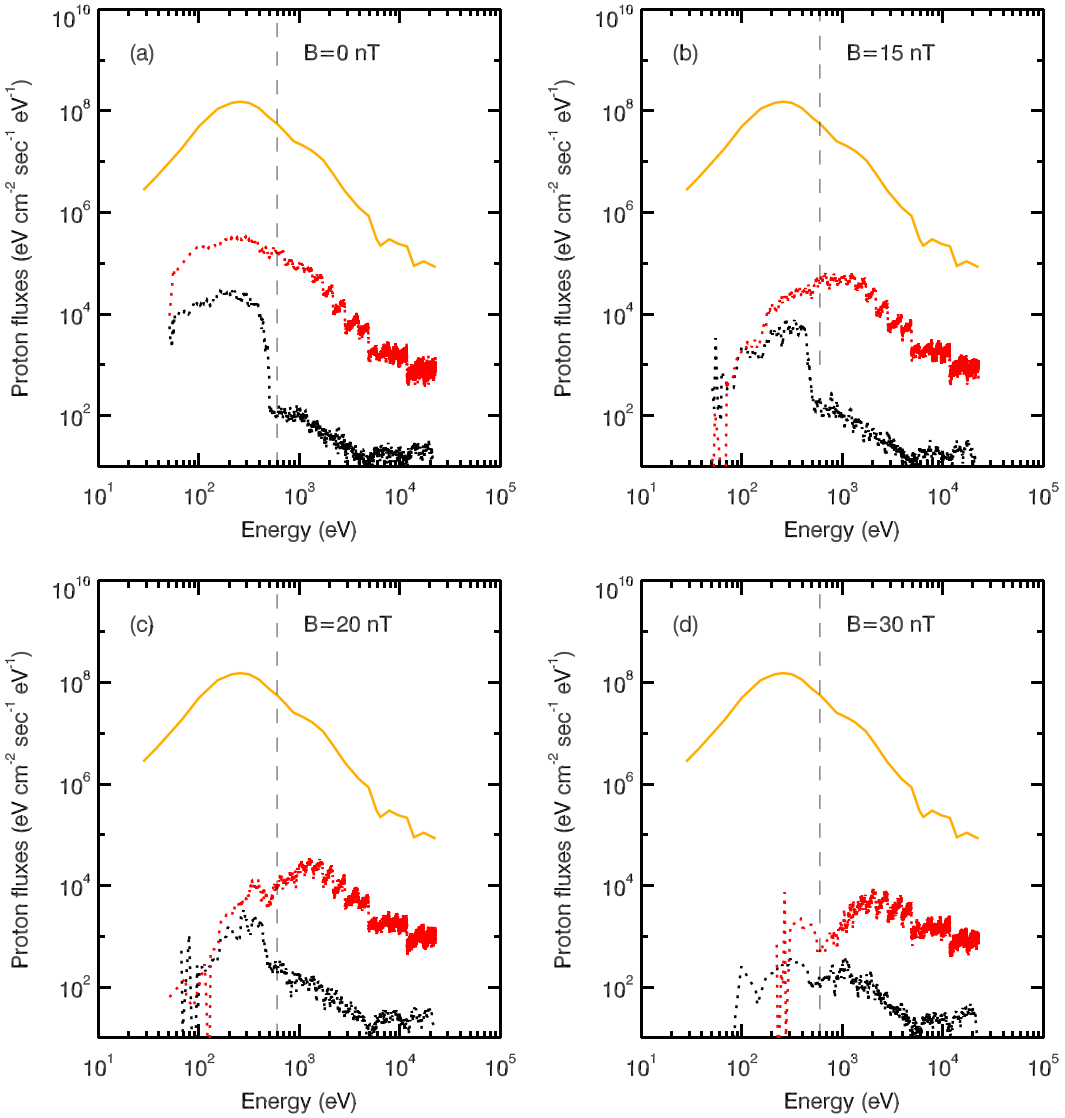

Figure 3. Upward (black line) and downward H^+ (red line) fluxes at 160 km for the case of proton precipitation (a) without and with an induced magnetic field (b) B = 15, (c) 20, and (d) 30 nT. The orange line shows the energy spectrum of the precipitating magnetosheath proton flux.

The calculated differential upward H and H^+ number fluxes at 500 km for cases without and with induced magnetic field B = 15, 20, and 30 nT are presented in Figure 4. The backscattered energy fluxes of H and H^+ are equal to 1.5% and 4.0%, respectively, in the absence of magnetic field. For B = 15 nT the backscattered energy fluxes are 0.7% and 19% of the incident energy flux, for B = 20 nT 0.4% and 25%, and for B = 30 nT 0.03% and 29% for H and H^+, respectively. As in the case of precipitating magnetosheath protons, the increase of the backscattered proton flux shows the same value (by a factor of 5–6) and is caused by the shielding effect of the horizontal component of induced magnetic field.

The upward and downward H^+ fluxes at 160 km for the cases without and with an induced magnetic field B = 15, 20, and 30 nT are shown in Figure 5. As can be seen in Figure 5, the downward fluxes of protons peak around 600 eV in the case of a precipitation of neutral hydrogen from solar wind. The backscattered fluxes of protons peak at energies slightly less than 600 eV because they are formed by collisional spreading in the Martian atmosphere that is accompanied by an energy depletion of the penetrating flux of hydrogen atoms. The peak at 600 eV in the H^+ spectra of backscattered flux at 500 km and the downward flux at 160 km is the result of charge exchange collisions between the precipitating neutral hydrogen spectrum (peaking at

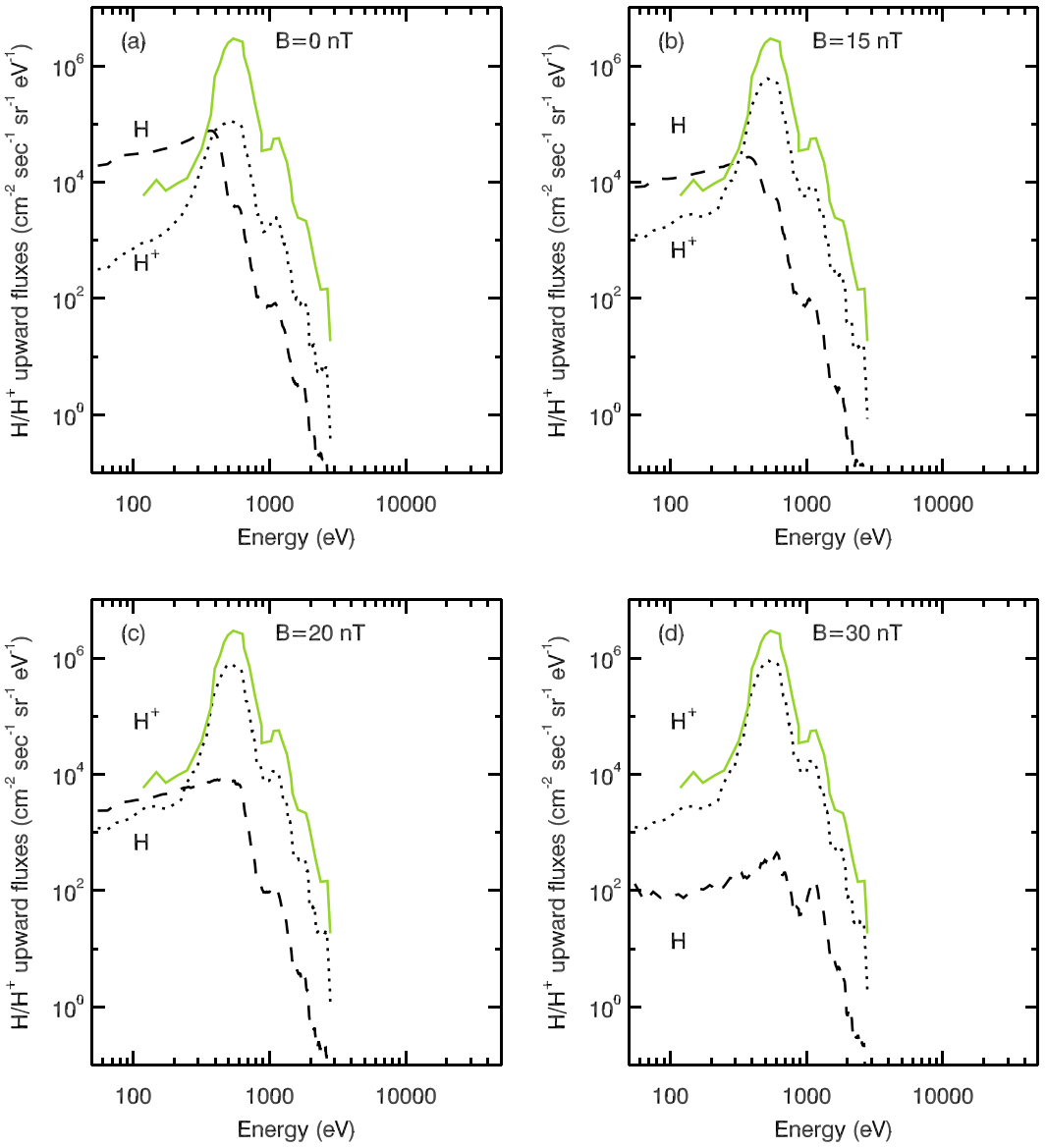

Figure 4. Upward H (dashed line) and H^+ (dotted line) fluxes at 500 km for the case of hydrogen precipitation (a) without and with an induced magnetic field (b) B = 15, (c) 20, and (d) 30 nT. The green line shows the energy spectrum of the precipitating hydrogen flux.

600 eV) with the planetary ions, which allows the new protons to keep the same direction and energy as the original neutral hydrogen atoms.

4. Discussion

The calculated backscattered (black line) and penetrating (red line) proton fluxes at 160 km are shown in Figure 6 for the case where both hydrogen and proton precipitation were taken into account without (a) and with induced magnetic field B = 15 (b), 20 (c), and 30 (d) nT. It is seen that the total fluxes show the same features as those produced by hydrogen precipitation. This confirms the idea that protons of the solar wind can play a dominant role in the proton auroral events. The energy of the peak of the downward flux does not depend on the induced magnetic field, while the flux value decreases with increasing B intensity. In the simulations the spectrum of the precipitating hydrogen atoms was taken equal to 1% of the angle-integrated ion spectrum from the solar wind. With this assumption the ratios of the peak values of the penetrating fluxes

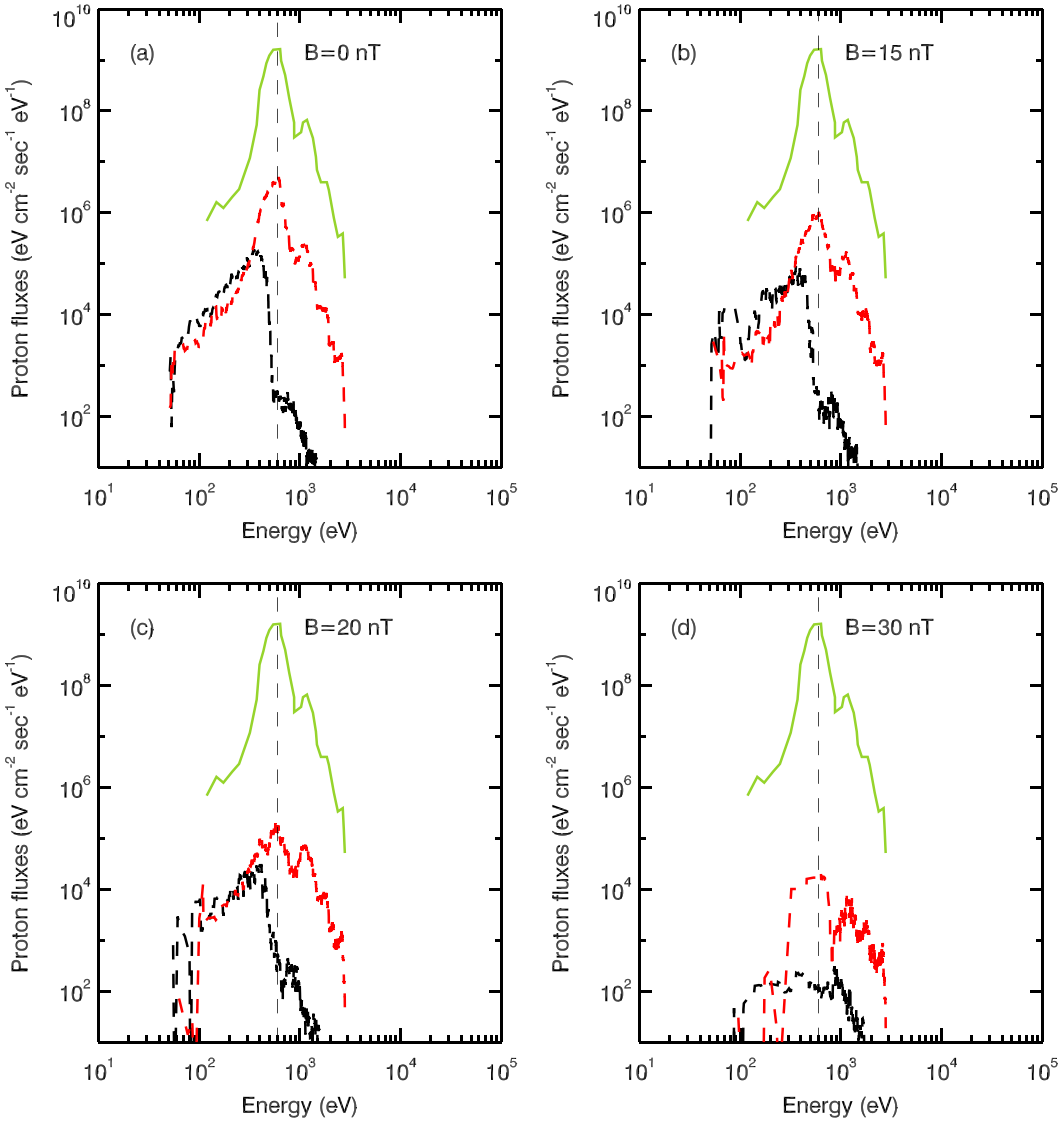

Figure 5. Upward (black line) and downward (red line) H^+ fluxes at 160 km for the case of hydrogen precipitation (a) without and with induced magnetic field (b) B = 15, (c) 20, and (d) 30 nT. The green line shows the energy spectrum of the precipitating hydrogen flux.

obtained in simulations to the measured ones (shown in Figure 1b as a red curve) are as follows: 11.5, 2.4, 0.5, and 0.05 for the B = 0, 15, 20, and 30-nT cases, respectively.

As we have simultaneous MAVEN observations of the downward fluxes and induced magnetic field, we have a possibility to estimate the efficiency of charge exchange between solar wind and extended hydrogen corona. According to Connerney et al. (2015), the value of the induced magnetic field is on the level of 10–15 nT. This implies that the efficiency of the conversion of the protons to hydrogen atoms should be a factor 3–5 less than 1%. For larger values of the magnetic field, the efficiency increases and will reach the level of 1%, for B~15–20 nT, and it could be as large as 20% for B = 30 nT.

An important point to discuss is the discrepancy between the shapes of calculated and measured fluxes at low altitudes. Indeed, the SWIA observations show an unexpected behavior of the wings of the downward proton flux spectra. Both the low energy (below peak, at $E < 400$ eV) and the high energy components (above peak, at $E > 800$ eV) of the backscattered flux exceed the downward proton flux (Figure 1b). The Monte Carlo simulations cannot reproduce this behavior. For the runs with induced magnetic field, the model calculations

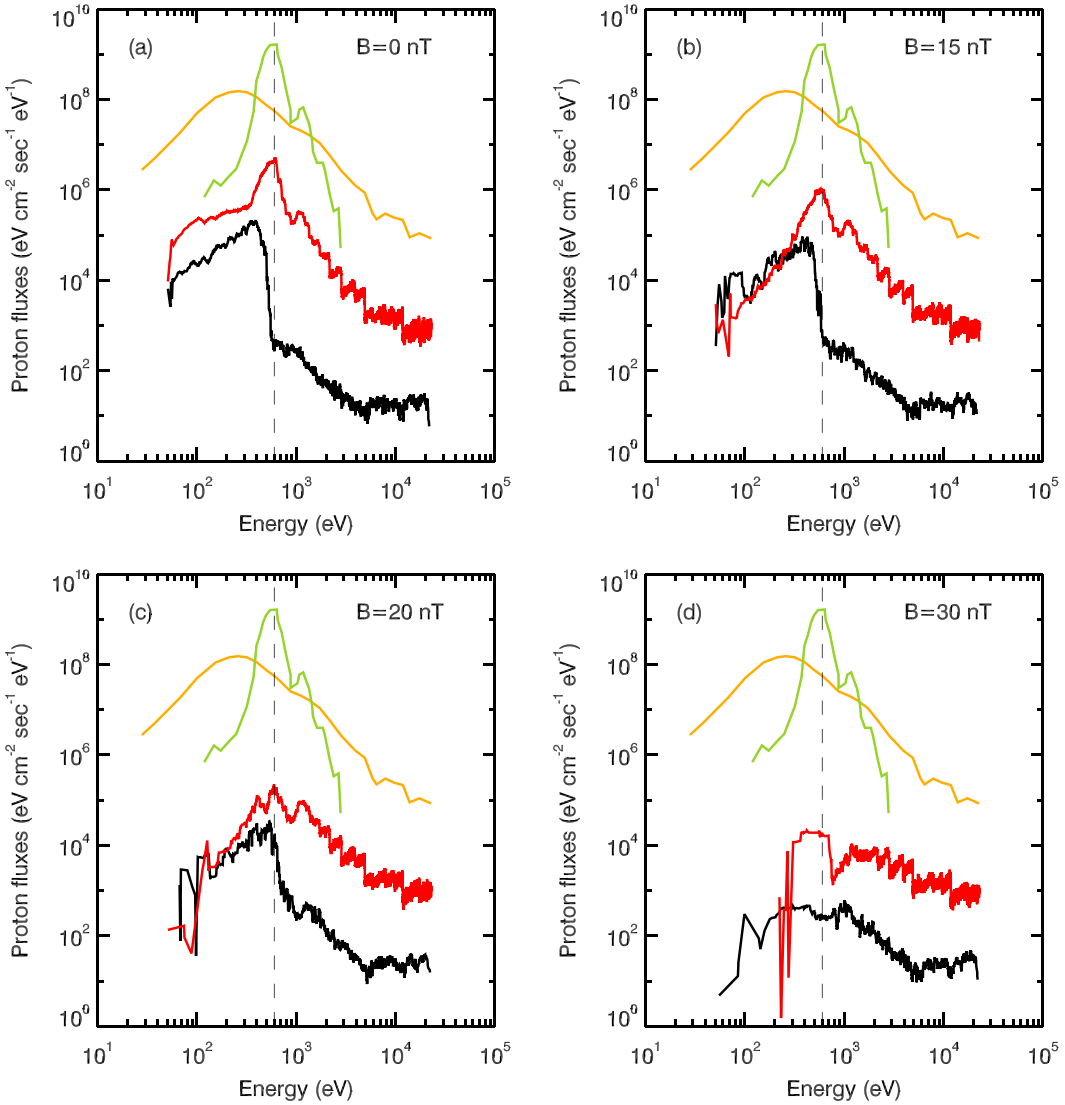

Figure 6. Upward (black line) and downward (red line) H^+ fluxes at 160 km for the case of both hydrogen and proton precipitation (a) without and with induced magnetic field (b) B = 15, (c) 20, and (d) 30 nT. The green and orange lines show the energy spectrum of the precipitating hydrogen and proton fluxes, respectively.

indicate (Figures 6b–6d) that at low energies the backscattered flux can be larger than the penetrating one. Comparison of the results presented in the study suggests that one possibility to explain the depletion of the low energy wing of the penetrating protons is their deflection at higher altitudes by the horizontal magnetic field preventing them from reaching the 160-km level. This is illustrated by the comparison of black and red curves in Figures 3 and 5. Nevertheless, the higher value of the backscattered flux was obtained just in small energy interval at low energies. For higher energies and in the higher energy wing, the modeled backscattered flux was always less than the penetrating one. It is important to note that in measurements, the slope of the high energetic wings (both in backscattered and penetrating fluxes) is less steep than those in the precipitating spectra at MAVEN periapsis, so the system should provide an additional (to the energy carried by the penetrating particles) physical process producing the high energetic particles.

Another important feature is that the large disagreement between simulations and measurements is in the relative magnitude of backscattered and penetrating fluxes at 160 km. In all runs the backscattered flux is always much less than the penetrating one and their ratio does not exceed the value of 3%. In the MAVEN observations the relative magnitude of the downward and upward fluxes is totally different. This is seen

in the plot of the penetrating and backscatter populations near periapsis for the 27 February orbit (Figure 1b), where the upward energy flux apparently exceeds the downward one. This case is not unique as it could be seen from right top panel in Figure 3 of Halekas, Lillis, et al. (2015), where the ratio of backscattered and downward fluxes is always higher than 0.1, and frequently more than 1. If these measurements are correct, the higher values of the upward flux relative to the downward flux also imply the existence of an energy reservoir supplying the upward flux. According to Halekas, Lillis, et al. (2015) two such potential energy reservoirs are the penetration of neutral hydrogen (not measured by SWIA-MAVEN) or the presence of electric currents. The role of H atom penetration can be evaluated from our simulations. The total energy stored in the precipitating flux is large enough to supply the upward flux, but its energy distribution significantly differs from the measurements. In addition, the simulations do not suggest that the interaction between the precipitating population and the atmosphere can produce a high-energy wing in the upward moving protons at 160 km (Figure 5). The role of the electric currents is not clear, but this effect is unlikely to be very large in an unmagnetized planet. An additional possible factor affecting the upward to downward flux ratio is the presence of a horizontal magnetic field. Indeed, simulations shown in Figures 3 and 5 indicate that the presence of the magnetic field reduces the downward flux at low energies more significantly than the upward flux, leading to a strong change in the ratio of the downward to upward fluxes at low energies. However, an important result is that our simulations never produce upward fluxes in the high-energy tail exceeding the downward flux at any energy. These results are thus in disagreement with the SWIA data, but they partially agree with the measurements showing a decrease of the upward/downward fluxes ratio with increasing energy.

5. Conclusions

The characteristics of the MAVEN orbit, with its low altitude periapsis, now make it possible to measure the proton energy spectrum of the upward and downward fluxes of protons down to about 160 km. The SWIA/MAVEN instrument frequently detects a low flux of positive ions traveling at a velocity equal to that of the upstream solar wind. Measurements of the ion composition with the STATIC instrument have shown (Brain et al., 2015) that these ions are protons, in agreement with the idea that these are H ENAs reconverted into protons as described earlier. The flux measurements have been compared for the first time with Monte Carlo simulations of the interaction of energetic protons and hydrogen ENAs with the upper atmosphere of Mars. The comparison of the flux and energy distributions of the downward and upward moving populations makes it possible to infer information on the characteristics of the upstream solar wind protons. In addition, the solar wind hydrogen deposition in the atmosphere may be inferred from the comparison of the charged fraction to the total H ENA abundance.

The results of simulations show that the efficiency of charge exchange between solar wind and the extended hydrogen corona can be evaluated from the comparison between simulations and measurements. The dominant role of the hydrogen precipitation allows to assume that the value of the peak of the energy flux of downward protons at lower altitudes is mainly defined by the flux of precipitating hydrogen. We also found a strong dependence of the value of the downward protons peak on the strength of the induced magnetic field. Assuming that the spectrum of the precipitating hydrogen atoms is equal to 1% of the angle-integrated ion spectrum from the solar wind, we obtain the following ratio of the peak values of the penetrating fluxes obtained in simulations to the measured ones: 11.5, 2.4, 0.5, and 0.05 for cases B = 0, 15, 20, and 30 nT, respectively. These results imply that for the case without magnetic field the efficiency of the conversion of the protons to hydrogen should be equal to 0.1%, for B = 15 nT 0.4%, at B = 20 nT 2%, and at B = 30 nT 20%. For the measured values of the induced magnetic field on the level of 10–15 nT (Connerney et al., 2015), the efficiency of the conversion of the protons to hydrogen is therefore estimated ~0.2–0.3%. Simultaneous observations of the magnetic field and downward fluxes allow estimating this value with rather high accuracy.

This study indicates that the presence of the induced horizontal magnetic field does not significantly modify the peak energy of the downward proton flux, but that the field intensity controls the total flux. The shape of the low- and high-energy tails of the calculated proton flux distribution at low altitude significantly differs from that reported from the SWIA instrument. The calculated low energy upward proton flux below 600 eV, unlike the SWIA measurements, remains less than the downward flux. Although the presence of the induced field somewhat affects the value of this low-energy upward flux, it is not sufficient to

reproduce the observed upward/downward ratio. An even more puzzling discrepancy is the large value of the high-energy tail of the upward flux relative to the downward proton flux. None of our simulations for proton or H ENA precipitation, with or without an induced magnetic field, is able to produce this feature, which implies the existence of an energy reservoir inside the ionosphere. The role of precipitation of fast H atoms has also been examined, but the simulations indicate that this H ENA population is equally unable to generate the proton high-energy tail described in the SWIA measurements of the upward moving protons near periapsis.

Finally, the expected characteristics of Lyman-α enhancements based on this model will also be compared with observations of recently discovered proton aurora (Deighan et al., 2016, AGU Fall meeting 2016; Ritter et al., 2018) in a future study.

Acknowledgments
D.B. and V.S. were supported by the Russian Science Foundation (project 18-12-00447). B.H. is supported by the Belgian Fund for Scientific Research (FNRS). This research was partly funded by the SCOOP-BRAIN program of the Belgian Federal Science Policy Office (BELSPO). The SWIA data used in this study are available from NASA.

References

Akalin, F., Morgan, D. D., Gurnett, D. A., Kirchner, D. L., Brain, D. A., Modolo, R., et al. (2010). Dayside induced magnetic field in the ionosphere of Mars. *Icarus*, *206*, 104–111. https://doi.org/10.1016/j.icarus.2009.03.021

Barabash, S., Lundin, R., Zarnowiecki, R., & Grzedzielski, S. (1995). Diagnostic of energetic neutral particles at Mars by the ASPERA-C instrument for the Mars 96 mission. *Advances in Space Research*, *16*(4), 81–86. https://doi.org/10.1016/0273-1177(95)00212-W

Bertaux, J.-L., Leblanc, F., Witasse, O., Quemerais, E., Lilensten, J., Stern, S. A., et al. (2005). Discovery of an aurora on Mars. *Nature*, *435*(7043), 790–794. https://doi.org/10.1038/nature03603

Bisikalo, D. V., Shematovich, V. I., & Gérard, J.-C. (1995). Kinetic model of the formation of the hot oxygen geocorona: 2. Influence of O^+ ion precipitation. *Journal of Geophysical Research*, *100*(A3), 3715–3720. https://doi.org/10.1029/94JA03196

Bisikalo, D. V., Shematovich, V. I., Gérard, J.-C., & Hubert, B. (2017). Influence of the crustal magnetic field on the Mars aurora electron flux and UV brightness. *Icarus*, *282*, 127–135. https://doi.org/10.1016/j.icarus.2016.08.035

Brain, D. A., Bagenal, F., Acuna, M. H., & Connerney, J. E. P. (2003). Martian magnetic morphology: Contributions from the solar wind and crust. *Journal of Geophysical Research*, *108*(A12), 1424. https://doi.org/10.1029/2002JA009482

Brain, D. A., McFadden, J. P., Halekas, J. S., Connerney, J. E. P., Bougher, S. W., Curry, S., et al. (2015). The spatial distribution of planetary ion fluxes near Mars observed by MAVEN. *Geophysical Research Letters*, *42*, 9142–9148. https://doi.org/10.1002/2015GL065293

Chaufray, J. Y., Bertaux, J.-L., Leblanc, F., & Quémerais, E. (2008). Observation of the hydrogen corona with SPICAM on Mars Express. *Icarus*, *195*(2), 598–613. https://doi.org/10.1016/j.icarus.2008.01.009

Connerney, J. E. P., Espley, J. R., DiBraccio, G. A., Gruesbeck, J. R., Oliversen, R. J., Mitchell, D. L., et al. (2015). First results of the MAVEN magnetic field investigation. *Geophysical Research Letters*, *42*, 8819–8827. https://doi.org/10.1002/2015GL065366

Deighan, J., Jain S. K., Chaffin, M. S., Fang, X., Halekas, J. S., Clarke, J. T., et al. (2016). Discovery of proton aurora at Mars. American Geophysical Union, fall general assembly 2016, Abstract P13D-01.

Diéval, C., Kallio, E., Barabash, S., Stenberg, G., Nilsson, H., Futaana, Y., et al. (2012). A case study of proton precipitation at Mars: Mars Express observations and hybrid simulations. *Journal of Geophysical Research*, *117*, A06222. https://doi.org/10.1029/2012JA017537

Diéval, C., Stenberg, G., Nilsson, H., & Barabash, S. (2013). A statistical study of proton precipitation onto the Martian upper atmosphere: Mars Express observations. *Journal of Geophysical Research: Space Physics*, *118*, 1972–1983. https://doi.org/10.1002/jgra.50229

Fox, J. L., & Hac, A. B. (2009). Photochemical escape of oxygen from Mars: A comparison of the exobase approximation to a Monte Carlo method. *Icarus*, *204*(2), 527–544. https://doi.org/10.1016/j.icarus.2009.07.005

Frey, H. U., Mende, S. B., Immel, T. J., Fuselier, S. A., Claflin, E. S., Gérard, J. C., & Hubert, B. (2002). Proton aurora in the cusp. *Journal of Geophysical Research*, *107*(A7), 1091. https://doi.org/10.1029/2001JA900161

Futaana, Y., Barabash, S., Grigoriev, A., Holmström, M., Kallio, E., Brandt, P. C., & Dierker, C. (2006). First ENA observations at Mars: ENA emissions from the Martian upper atmosphere. *Icarus*, *182*(2), 424–430. https://doi.org/10.1016/j.icarus.2005.09.019

Galli, A., Wurz, P., Kallio, E., Ekenbäck, A., Holmström, M., Barabash, S., et al. (2008). Tailward flow of energetic neutral atoms observed at Mars. *Journal of Geophysical Research*, *113*, E12012. https://doi.org/10.1029/2008JE003139

Gérard, J.-C., Hubert, B., Bisikalo, D. V., & Shematovich, V. I. (2000). A model of the Lyman-αline profile in the proton aurora. *Journal of Geophysical Research*, *105*(A7), 15,795–15,805. https://doi.org/10.1029/1999JA002002

Gérard, J.-C., Hubert, B., Meurant, M., Shematovich, V. I., Bisikalo, D. V., Frey, H., et al. (2001). Observation of the proton aurora with IMAGE FUV imager and simultaneous ion flux in situ measurements. *Journal of Geophysical Research*, *106*(A12), 28,939–28,948. https://doi.org/10.1029/2001JA900119

Gérard, J.-C., Soret, L., Libert, L., Lundin, R., Stiepen, A., Radioti, A., & Bertaux, J.-L. (2015). Concurrent observations of ultraviolet aurora and energetic electron precipitation with Mars Express. *Journal of Geophysical Research: Space Physics*, *120*, 6749–6765. https://doi.org/10.1002/2015JA021150

Gunell, H., Brinkfeldt, K., Holmström, M., Brandt, P. C., Barabash, S., Kallio, E., et al. (2006). First ENA observations at Mars: Charge exchange ENAs produced in the magnetosheath. *Icarus*, *182*(2), 431–438. https://doi.org/10.1016/j.icarus.2005.10.027

Halekas, J. S., Lillis, R. J., Mitchell, D. L., Cravens, T. E., Mazelle, C., Connerney, J. E. P., et al. (2015). MAVEN observations of solar wind hydrogen deposition in the atmosphere of Mars. *Geophysical Research Letters*, *42*, 8901–8909. https://doi.org/10.1002/2015GL064693

Halekas, J. S., Taylor, E. R., Dalton, G., Johnson, G., Curtis, D. W., McFadden, J. P., et al. (2015). The Solar Wind Ion Analyzer for MAVEN. *Space Science Reviews*, *195*(1-4), 125–151. https://doi.org/10.1007/s11214-013-0029-z

Holmström, M., Barabash, S., & Kallio, E. (2002). Energetic neutral atoms at Mars 1: Imaging of solar wind protons. *Journal of Geophysical Research*, *107*(A10), 1277. https://doi.org/10.1029/2001JA000325

Kallio, E., & Barabash, S. (2001). Atmospheric effects of precipitating energetic hydrogen atoms on the Martian atmosphere. *Journal of Geophysical Research*, *106*(A1), 165–177. https://doi.org/10.1029/2000JA002003

Kallio, E., Luhmann, J. G., & Barabash, S. (1997). Charge exchange near Mars: The solar wind absorption and energetic neutral atom production. *Journal of Geophysical Research*, *102*(A10), 22,183–22,197. https://doi.org/10.1029/97JA01662

Leblanc, F., Chaufray, J. Y., Witasse, O., Lilensten, J., & Bertaux, J.-L. (2006). The Martian dayglow as seen by SPICAM UV spectrometer on Mars Express. *Journal of Geophysical Research*, *111*, E09S11. https://doi.org/10.1029/2005JE002664

Mura, A., Orsini, S., Milillo, A., Kallio, E., Galli, A., Barabash, S., et al. (2008). ENA detection on the dayside of Mars: ASPERA-3 NPD statistical study. *Planetary and Space Science*, *56*(6), 840–845. https://doi.org/10.1016/j.pss.2007.12.013

Ritter, B., Gérard, J.-C., Hubert, B., & Rodriguez, L. (2018). Observations of the Proton Aurora on Mars with SPICAM on board Mars Express. *Geophysical Research Letters*, *45*, 612–619. https://doi.org/10.1002/2017GL076235

Schneider, N. M., Deighan, J. I., Jain, S. K., Stiepen, A., Stewart, A. I. F., Larson, D., et al. (2015). Discovery of diffuse aurora on Mars. id. 0313. *Science*, *350*(6261), 0313. https://doi.org/10.1126/science.aad0313

Shematovich, V. I. (2008). Kinetics of suprathermal atoms and molecules in the rarefied planetary atmospheres. In T. Abe (Ed.), *Rarefied Gas Dynamics, AIP Conference. Proceedings* (Vol.1084, pp. 1047–1054). https://doi.org/10.1063/1.3076436

Shematovich, V. I., Bisikalo, D. V., Diéval, C., Barabash, S., Stenberg, G., Nilsson, H., & Gérard, J.-C. (2011). Proton and hydrogen atom transport in the Martian upper atmosphere with an induced magnetic field. *Journal of Geophysical Research*, *116*, A11320. https://doi.org/10.1029/2011JA017007

Shematovich, V. I., Bisikalo, D. V., & Gérard, J.-C. (1994). A kinetic model of the formation of the hot oxygen geocorona: 1. Quiet geomagnetic conditions. *Journal of Geophysical Research*, *99*(A12), 23,217–23,228. https://doi.org/10.1029/94JA01769

Shematovich, V. I., Bisikalo, D. V., Gérard, J.-C., & Hubert, B. (2017). Changes in the Martian atmosphere induced by auroral electron precipitation. *Solar System Research*, *51*(5), 362–372. https://doi.org/10.1134/S0038094617050094

Soret, L., Gérard, J. C., Libert, L., Shematovich, V. I., Bisikalo, D. V., Stiepen, A., & Bertaux, J. L. (2016). SPICAM observations and modeling of Mars aurorae. *Icarus*, *264*, 398–406. https://doi.org/10.1016/j.icarus.2015.09.023

Stephan, A. W., Chakrabarti, S., & Cotton, D. I. M. (2000). Evidence of ENA precipitation in the EUV dayglow. *Geophysical Research Letters*, *27*(18), 2865–2868. https://doi.org/10.1029/2000GL000040

Wang, X.-D., Barabash, S., Futaana, Y., Grigoriev, A., & Wurz, P. (2013). Directionality and variability of energetic neutral hydrogen fluxes observed by Mars Express. *Journal of Geophysical Research: Space Physics*, *118*, 7635–7642. https://doi.org/10.1002/2013JA018876

Wang, X.-D., Barabash, S., Futaana, Y., Grigoriev, A., & Wurz, P. (2014). Influence of Martian crustal magnetic anomalies on the emission of energetic neutral hydrogen atoms. *Journal of Geophysical Research: Space Physics*, *119*, 8600–8609. https://doi.org/10.1002/2014JA020307